INTERNATIONAL JOURNAL FOR NUMERICAL METHODS IN FLUIDS, VOL. 12, 637–653 (1991)

COMPUTATIONS FOR A JET IMPINGING OBLIQUELY ON A FLAT SURFACE

SHU-HAO CHUANG AND CHING-YUAN WEI

Department of Mechanical Engineering, National Chung-Hsing University, Taichung, Taiwan 40227, R.O.C.

SUMMARY

A SIMPLE-C algorithm and Jones–Launder k–ε two-equation turbulence model are used to simulate a two-dimensional jet impinging obliquely on a flat surface. Both the continuity and momentum equations for the unsteady state are cast into suitable finite difference equations. The pressure, velocity, turbulent kinetic energy and turbulent energy dissipation rate distributions are solved and show good agreement with various experimental data. The calculations show that the flow field structure of the jet impinging obliquely on a flat surface is strongly affected by the oblique impingement angle. The maximum pressure zone of the obliquely impinging jet flow field moves towards the left as the oblique impingement angle is decreased.

KEY WORDS Obliquely impinging jet Oblique impingement angle SIMPLE-C algorithm

INTRODUCTION

The fan-powered vertical-take-off-and-landing (VTOL) military aircraft has increasingly required improved numerical simulation methods to predict its performance, particularly with regard to propulsion-induced aerodynamic effects in the hover mode of VTOL flight. The problem is not an easy one since the hover mode of a VTOL aircraft is characterized by complicated flow field phenomena. Special attention has to be paid to the effect of the single, planar, unvectored lift jet on the ground surface.[1] The jet exits from a slot of width D in a contoured upper surface at a distance H above the ground plane, as shown in Figure 1. The two-dimensional normally or obliquely impinging jet flow field can be characterized by the following three regions:[1] the free jet region in which the flow is essentially the same as that of a jet issuing into an unbounded region; the impingement region in which the flow changes direction with a large pressure gradient; and the wall–jet region in which the flow traverses the ground surface.

Solutions for a plane turbulent impinging jet prior to 1970 were reviewed by Wolfshtein.[2] Experimental measurements of an impinging jet with a round nozzle were made by Coleman,[3] who found that the flow was essentially characterized by the above three regions. The static pressure distribution of the ground plane in the impingement region has been solved by the frozen vorticity concept.[4] Theoretical analyses of impinging jet flow have been concerned with finding solutions for several separate regions and then combining these into a complete solution.[5,6] The advantage of this procedure is that it enables one to select an adaptive model for each separate region, thus avoiding the complex problem.

The two-dimensional Navier–Stokes equations with ground effects were studied by Bower and Kotansky,[7] who first utilized the augmented central difference and one-equation turbulence model to simulate impinging jet flow. In order to study the interaction between lift jet and ground

0271–2091/91/070637–17$08.50

Received July 1989
Revised May 1990

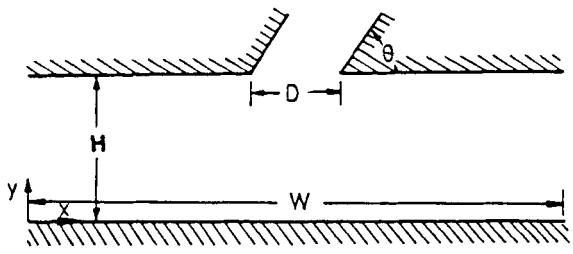

Figure 1. Basic configuration of obliquely impinging jet

plane for VTOL aircraft, one needs to use experimental measurements and numerical computation to investigate the effect of impinging jet flow on various upper flat-plate profiles.[8] Two- and three-dimensional impinging jet flows were studied by Bower and co-workers, [9,10] who utilized the streamfunction–vorticity and Jones–Launder k–ε two-equation turbulence model. Their results showed good agreement between numerical predictions and experimental data. Incompressible, inviscid, rotational impingement problems have also been considered;[11] the computations for two-dimensional, axisymmetric, normally impinging and obliquely impinging jets compared well with observations. Agarwal and Bower[12] and Looney and Walsh[13] used the same turbulence model and compressible equations as Rubel[11] to predict impinging jet flow and also found good agreement with experimental results. The above solution methods were limited to the use of streamfunction–vorticity for solving the Navier–Stokes equations.

In order to further understand the structure of impinging jet flow, one needs to use primitive variables for the solution. In viscous flow the fine mesh spacing makes the MacCormack scheme with the explicit method[14,15] extremely costly. Implicit methods[16,17] make the use of a large time step possible but require the inversion of block tridiagonal matrices. Numerical simulation of impinging jet flow by the Beam–Warming[16] method was done by Hwang and Liu.[18] A method developed by MacCormack[19] eliminated the inversion disadvantage by introducing a predictor–corrector scheme. Unfortunately, this method was demonstrated only for a simple case. Numerical simulation of an impinging jet on a flat plate by the Lavante–Thompkins[20] method was performed by Chuang.[1] These numerical methods have some disadvantages; namely, the Jacobians of the co-ordinate transformation and dissipation terms often make the solution divergent because these terms are the flow variables. In addition, the primitive solutions for the inversion of the co-ordinate transformation are also very difficult, especially in a complex geometry flow field.

In order to overcome these disadvantages, in this paper we provide a well-known numerical method, i.e. the SIMPLE-C algorithm,[21] to solve the two-dimensional viscous compressible flow of a jet impinging obliquely on a flat plate, where the oblique impingement angle θ is in the range $90° \leqslant \theta \leqslant 50°$. Some of the results are compared with experimental data ($\theta = 90°, 80°, 70°$)[10,12,22,23] and found to be good in agreement. The oblique impingement angle is seen to a strong parameter for impinging jet flow in the present observations.

THEORETICAL MODEL

Assumptions

In order to simplify the study, the following assumptions are made.

1. The flow is that of a single two-dimensional obliquely impinging jet.
2. Both the upper plate surface and the ground plane are adiabatic and thermal effects on the viscosity are not considered.

3. Gravitational effects are not considered.
4. Cross-flow is not coupled with the impinging jet flow.

Governing equations

The general form of the transport equation for the unsteady two-dimensional compressible Navier–Stokes equations can be written as[24]

$$\frac{\partial(\rho\phi)}{\partial t}+\frac{\partial(\rho u\phi)}{\partial x}+\frac{\partial(\rho v\phi)}{\partial y}-\frac{\partial}{\partial x}\left(\Gamma\frac{\partial\phi}{\partial x}\right)-\frac{\partial}{\partial y}\left(\Gamma\frac{\partial\phi}{\partial y}\right)=S, \tag{1}$$

where the transfer coefficient Γ, the source term S and the transport variable ϕ are as defined in Table I. The total effective viscosity of the flow is

$$\mu_e=\mu_l+\mu_t,$$

where μ_l and μ_t are the molecular and eddy viscosity respectively and μ_t is known from the k–ε turbulence model as[25]

$$\mu_t=C_\mu\rho k^2/\varepsilon.$$

NUMERICAL METHOD

For the unsteady Navier–Stokes equations the time variation is taken to be of parabolic type and the space variation of elliptic type. Hence time marching and space iteration were used.

The difficulty in solving the Navier–Stokes equations is that the non-linear term and the pressure term are unknown. In order to solve the main variables u, v and p, Patankar[26] and

Table I. Governing equation variables

ϕ	Γ	S	S_p/V	S_c/V
u	μ_e	$-\dfrac{\partial p}{\partial x}+S^u$	0	$S^u-\dfrac{\partial p}{\partial x}$
v	μ_e	$-\dfrac{\partial p}{\partial y}+S^v$	0	$S^v-\dfrac{\partial p}{\partial y}$
k	$\dfrac{\mu_e}{\sigma_k}$	$G-\rho\varepsilon$	$-\dfrac{C_\mu\rho^2 k}{\mu_e}$	G
ε	$\dfrac{\mu_e}{\sigma_\varepsilon}$	$\dfrac{C_1\varepsilon G-C_2\rho\varepsilon^2}{k}$	$-\dfrac{C_2\rho\varepsilon}{k}$	$\dfrac{C_1 G\varepsilon}{k}$

$C_1=1{\cdot}44,\quad C_2=1{\cdot}72,\quad C_\mu=0{\cdot}09,\quad \sigma_k=1{\cdot}0,\quad \sigma_\varepsilon=1{\cdot}3$

$$S^u=\frac{\partial}{\partial x}\left(\mu_e\frac{\partial u}{\partial x}\right)+\frac{\partial}{\partial y}\left(\mu_e\frac{\partial v}{\partial y}\right)-\frac{2}{3}\frac{\partial}{\partial x}\left[\mu_e\left(\frac{\partial u}{\partial x}+\frac{\partial v}{\partial y}\right)+\rho k\right]$$

$$S^v=\frac{\partial}{\partial x}\left(\mu_e\frac{\partial u}{\partial y}\right)+\frac{\partial}{\partial y}\left(\mu_e\frac{\partial v}{\partial y}\right)-\frac{2}{3}\frac{\partial}{\partial y}\left[\mu_e\left(\frac{\partial u}{\partial x}+\frac{\partial v}{\partial y}\right)+\rho k\right]$$

$$G=\mu_e\left\{2\left[\left(\frac{\partial u}{\partial x}\right)^2+\left(\frac{\partial v}{\partial y}\right)^2\right]+\left(\frac{\partial u}{\partial x}+\frac{\partial v}{\partial y}\right)^2\right\}$$

Spalding introduced the SIMPLE algorithm technique. The SIMPLE-C (SIMPLE-consistent) algorithm subsequently developed by van Doormaal and Raithby[21] and Latimer and Pollard[27] has a better residual mass convergence rate than the SIMPLE algorithm.[28] The present calculations are performed using the SIMPLE-C algorithm and a power-law scheme.

Finite difference equations

Integration over a control volume cell was used to construct the finite difference equations. First the general form of equation (1) can be rewritten as

$$\frac{\partial(\rho\phi)}{\partial t}+\frac{\partial J_x}{\partial x}+\frac{\partial J_y}{\partial y}=S, \tag{2}$$

where

$$J_x=\rho u\phi-\Gamma\frac{\partial\phi}{\partial x}, \qquad J_y=\rho v\phi-\Gamma\frac{\partial\phi}{\partial y}.$$

Integration over the control volume for (1) gives

$$\int\int\int_V\left(\frac{\partial(\rho\phi)}{\partial t}+\frac{\partial J_x}{\partial x}+\frac{\partial J_y}{\partial y}\right)\mathrm{d}V=\int\int\int_V S\,\mathrm{d}V, \tag{3}$$

where $\mathrm{d}V=\mathrm{d}x\,\mathrm{d}y\,\mathrm{d}z=\mathrm{d}x\,\mathrm{d}y$. The finite difference equation for (3) with a linearized source term is given as

$$\frac{(\rho_\mathrm{p}\phi_\mathrm{p}-\rho_\mathrm{p}^\circ\phi_\mathrm{p}^\circ)\Delta x\Delta y}{\Delta t}+J_\mathrm{e}-J_\mathrm{w}+J_\mathrm{n}-J_\mathrm{s}=(S_\mathrm{p}\phi_\mathrm{p}+S_\mathrm{c})\Delta x\Delta y, \tag{4}$$

where

$$J_i=\int J_x\mathrm{d}y\Big|_{\text{over interface } i} \qquad (i=\mathrm{e},\mathrm{w}),$$

$$J_i=\int J_y\mathrm{d}x\Big|_{\text{over interface } i} \qquad (i=\mathrm{n},\mathrm{s}).$$

Integration over a control volume cell for the continuity equation gives

$$\frac{(\rho_\mathrm{p}-\rho_\mathrm{p}^\circ)\Delta x\Delta y}{\Delta t}+F_\mathrm{e}-F_\mathrm{w}+F_\mathrm{n}-F_\mathrm{s}=0. \tag{5}$$

Subtracting (5) multiplied by ϕ_p from (4) gives

$$\rho_\mathrm{p}^\circ(\phi_\mathrm{p}-\phi_\mathrm{p}^\circ)\frac{\Delta x\Delta y}{\Delta t}+(J_\mathrm{e}-F_\mathrm{e}\phi_\mathrm{p})-(J_\mathrm{w}-F_\mathrm{w}\phi_\mathrm{p})+(J_\mathrm{n}-F_\mathrm{n}\phi_\mathrm{p})-(J_\mathrm{s}-F_\mathrm{s}\phi_\mathrm{p})=(S_\mathrm{p}\phi_\mathrm{p}+S_\mathrm{c})\Delta x\Delta y, \tag{6}$$

where F_i is the mass flow rate for surface i of the control volume. Then the total flux of a control volume cell can be written as

$$\begin{aligned} J_i-F_i\phi_\mathrm{p}&=a_i(\phi_\mathrm{p}-\phi_i) \quad (i=\mathrm{e},\mathrm{n}),\\ J_i-F_i\phi_\mathrm{p}&=a_i(\phi_i-\phi_\mathrm{p}) \quad (i=\mathrm{w},\mathrm{s}), \end{aligned} \tag{7}$$

where

$$a_i = D_i A(|P_i|) + [-F_i, 0] \quad (i = \mathrm{e, n}),$$
$$a_i = D_i A(|P_i|) + [F_i, 0] \quad (i = \mathrm{w, s}),$$

$P_i (= F_i/D_i)$ is the Peclet number for surface i, $A(|P_i|)$ is a function of P_i and $D_i = \Gamma_i A_i/(\delta x)_i$. Substituting these relations into (6), we obtain

$$a_\mathrm{p}\phi_\mathrm{p} = a_\mathrm{e}\phi_\mathrm{e} + a_\mathrm{w}\phi_\mathrm{w} + a_\mathrm{s}\phi_\mathrm{s} + a_\mathrm{n}\phi_\mathrm{n} + b, \tag{8}$$

where

$$b = S_\mathrm{c}\Delta x\Delta y + a_\mathrm{p}^\mathrm{o}\phi_\mathrm{p}^\mathrm{o},$$
$$a_\mathrm{p}^\mathrm{o} = \rho_\mathrm{p}^\mathrm{o}\Delta x\Delta y/\Delta t,$$
$$a_\mathrm{p} = a_\mathrm{e} + a_\mathrm{w} + a_\mathrm{s} + a_\mathrm{n} + a_\mathrm{p}^0 - S_\mathrm{p}\Delta x\Delta y.$$

Solution technique

The SIMPLE-C algorithm with a power-law scheme[26] was used to treat the problem. The power-law scheme is described as follows:[26]

$$\begin{aligned}
P_\mathrm{e} &> -10, & a_\mathrm{e}/D_\mathrm{e} &= -P_\mathrm{e},\\
-10 < P_\mathrm{e} &< 0, & a_\mathrm{e}/D_\mathrm{e} &= (1 + 0{\cdot}1\,P_\mathrm{e})^5 - P_\mathrm{e},\\
0 < P_\mathrm{e} &< 10, & a_\mathrm{e}/D_\mathrm{e} &= (1 - 0{\cdot}1\,P_\mathrm{e})^5,\\
P_\mathrm{e} &> 10, & a_\mathrm{e}/D_\mathrm{e} &= 0.
\end{aligned}$$

The general form can be written as

$$a_\mathrm{e} = D_\mathrm{e}[0, (1 - 0{\cdot}1|F_\mathrm{e}|/D_\mathrm{e})^5] + [0, -F_\mathrm{e}].$$

The same procedure is used for a_w, a_s, and a_n. Details of the SIMPLE-C algorithm[21,27] calculation procedures will not be repeated here. The TDMA and line-by-line sweep process was used at each time step iteration to calculate the governing non-linear finite difference equations. Underrelaxation was used at each time step to accelerate convergence. The underrelaxation factors used in the present calculations are shown in Table II.

Initial values and boundary conditions

Initial values must be given for the time-marching method and boundary conditions for the space iteration method.

Initial values. The velocity, kinetic energy and turbulence energy dissipation rate were taken as zero except for the inlet condition and relative pressure.

Table II. Underrelaxation factors f

u	v	k	ε	p	μ_t
0·2	0·2	0·3	0·3	0·4	0·4

Boundary conditions

At the inlet

(a) A uniform initial inlet velocity was used:

$$u = V_{in}\cos\theta, \qquad v = V_{in}\sin\theta,$$
$$k = 0{\cdot}003\,V_{in}^2, \qquad \varepsilon = C_\mu k^{3/2}/0{\cdot}03(D/2).$$

(b) An initial nozzle velocity profile was chosen from Reference 12:

$$\left.\begin{aligned} u &= V_{in}\cos\theta \\ v &= V_{in}\sin\theta \end{aligned}\right\} \quad x/D \leqslant 3{\cdot}83,$$

$$\left.\begin{aligned} u &= V_{in}\cos\theta(-1200x^2+360x+120)/147 \\ v &= V_{in}\sin\theta(-1200x^2+360x+120)/147 \end{aligned}\right\} \quad 3{\cdot}83 \leqslant x/D \leqslant 4{\cdot}18,$$

$$\left.\begin{aligned} u &= 0 \\ v &= 0 \end{aligned}\right\} \quad x/D \geqslant 4{\cdot}18,$$

$$k = 0{\cdot}003\,(u^2+v^2), \qquad \varepsilon = C_\mu k^{3/2}/0{\cdot}03(D/2).$$

At the outlet

$$\partial\phi/\partial x = 0, \qquad v = 0$$

($\phi = u, k, \varepsilon, p$; assuming fully developed flow).

At the wall

$$u = 0, \qquad v = 0$$

(no-slip conditions); k and ε were handled by the wall function.[25,29,30]

Grid system

A staggered grid[26] arrangement of integration over the control volume was used to avoid wavy phenomena: x-direction—non-uniform grid, expanding the stretching factor (RATIO) along both sides from the nozzle centre, with RATIO = 1·05–1·25 (64 grid points); y-direction—uniform grid (68 grid points).

RESULTS AND DISCUSSION

In the present analysis the parameters are $\theta = 90°$–$50°$, $H = 2$, $W = 7{\cdot}36$ and $Re = 2 \times 10^4$. The convergence rate of residual mass with time marching is shown in Figure 2. Two recirculation regions of complex structure were formed on either side of the impinging jet flow as shown in Figure 3. The centreline velocity decay for the normally impinging jet is shown in Figure 4. The present results with an initial velocity profile chosen from Reference 12 (case (b)) are in good agreement with the experimental data of Bower *et al.*[10] The centreline velocity with a uniform initial velocity profile (case (a)) is slightly higher than that of the experimental data; this is attributed errors arising from viscous effects due to nozzle contraction. The same phenomenon was also found in the numerical prediction of Law and Masliyah[31] and van Heiningen *et al.*[32] The centreline pressure distribution shown in Figure 5 can also explain this phenomenon.

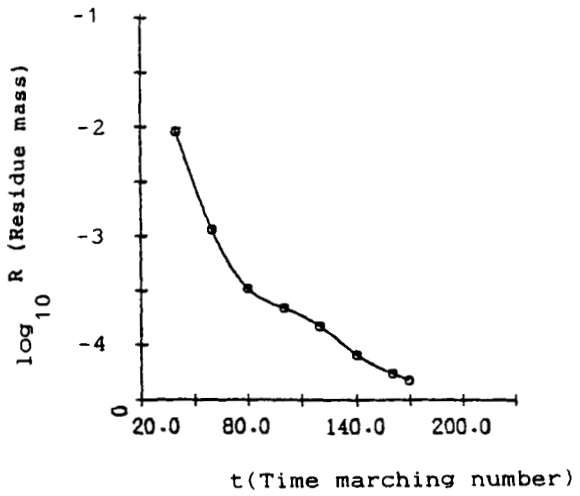

Figure 2. Convergence rate ($\Delta t = 0{\cdot}02$)

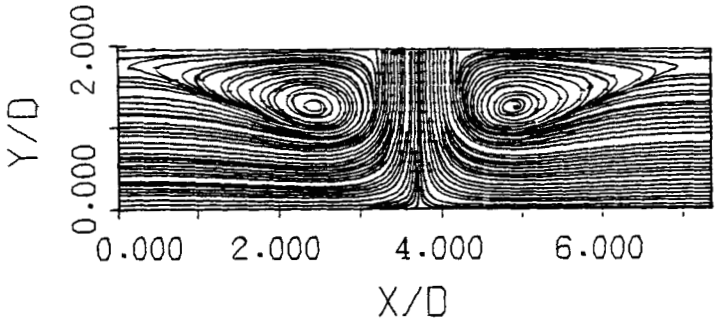

Figure 3. Streamline flow pattern for $\theta = 90°$

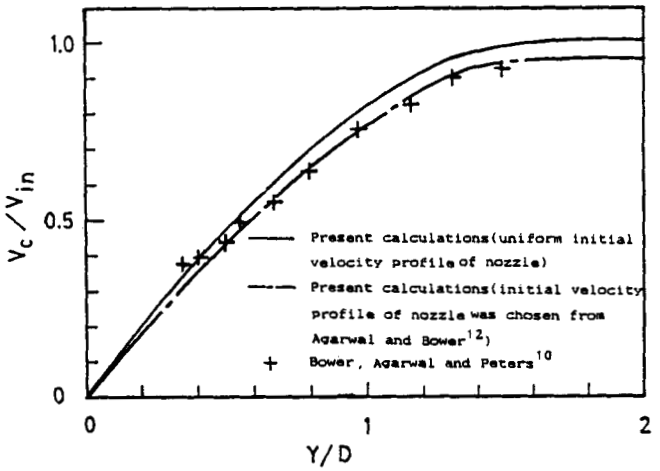

Figure 4. Centreline velocity decay for $\theta = 90°$

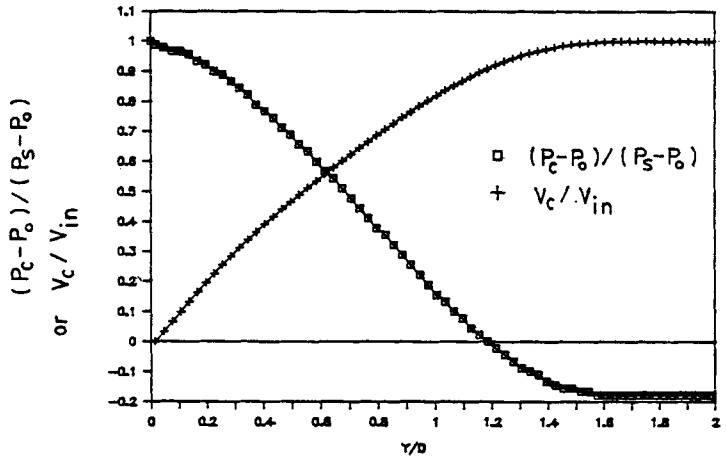

Figure 5. Centreline pressure and velocity distributions for $\theta = 90°$

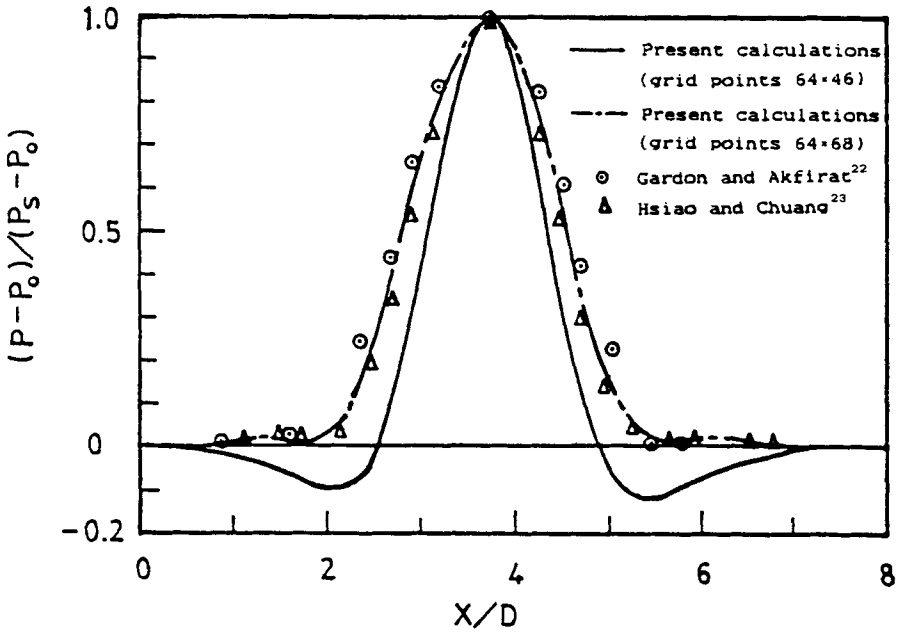

Figure 6. Ground plane pressure distributions for $\theta = 90°$

The computed pressure distribution of the ground plane for 64×68 grid points is compared with the experimental data of Gardon and Akfirat[22] and Hsiao and Chuang[23] in Figure 6 and found to be in good agreement. The ground plane pressure distribution for 64×46 grid points is also shown in Figure 6. The calculated results deviate from the experimental data in this case, particularly downstream of the ground plane, owing to the diffusion error of grid points with large grid size. The pressure contours of the normally impinging jet flow are shown in Figure 7. A larger pressure and pressrue gradient are seen in the impingement region, with lower pressure

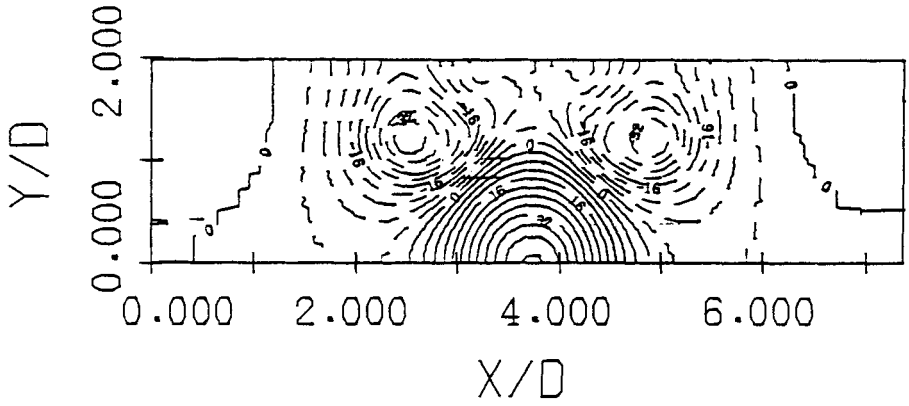

Figure 7. Pressure contours for $\theta = 90°$; broken lines indicate negative pressure

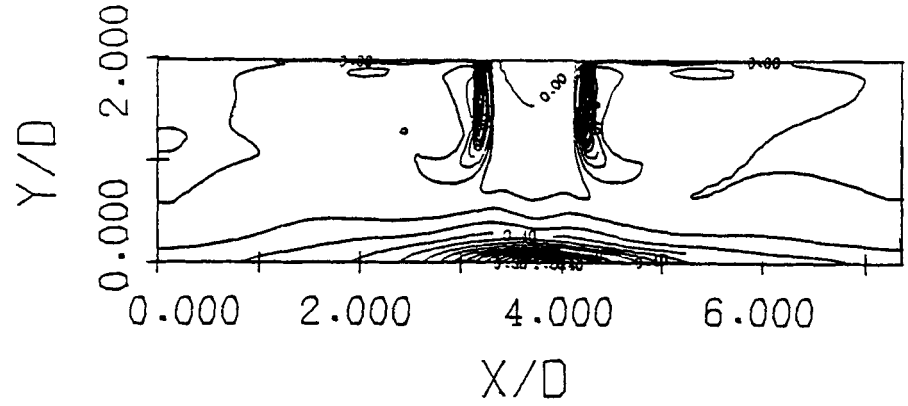

Figure 8. Turbulent kinetic energy contours for $\theta = 90°$

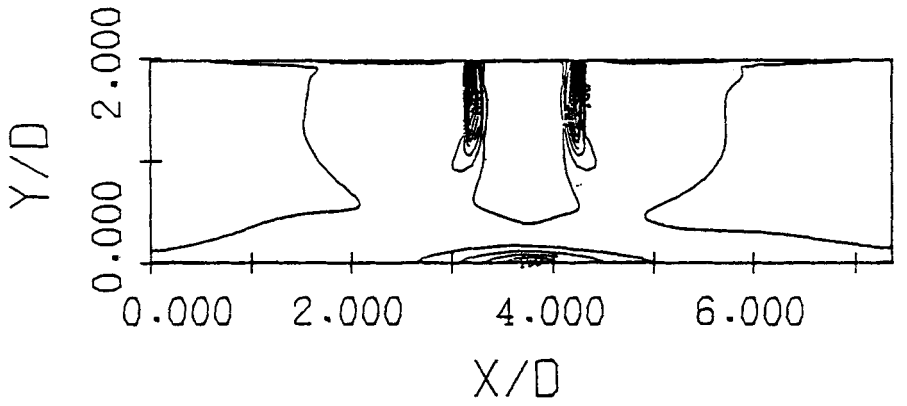

Figure 9. Turbulent energy dissipation rate contours for $\theta = 90°$

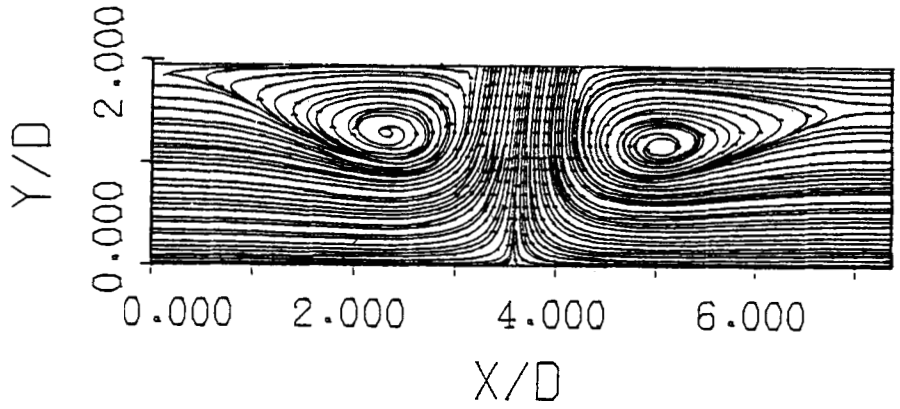

Figure 10. Streamline flow pattern for $\theta = 80°$

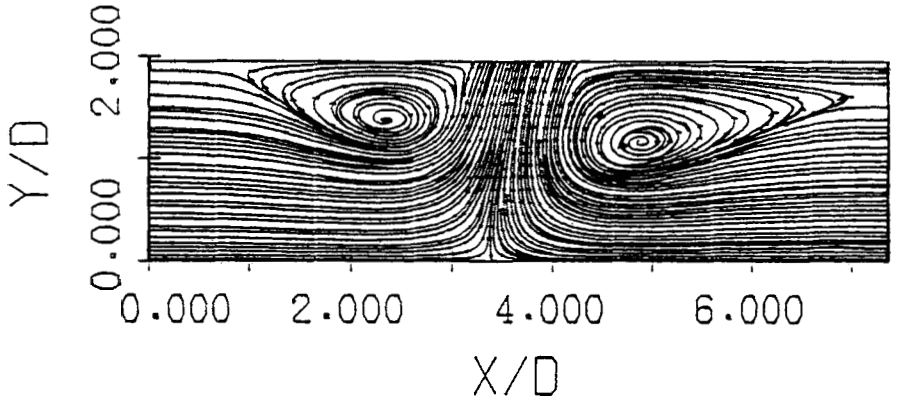

Figure 11. Streamline flow pattern for $\theta = 70°$

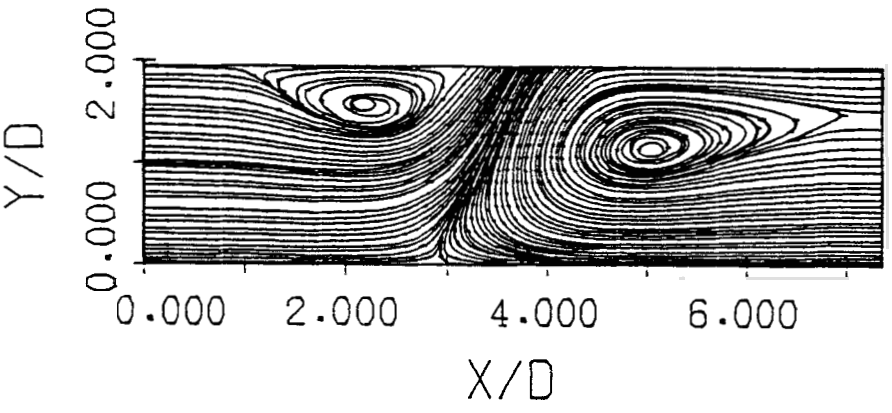

Figure 12. Streamline flow pattern for $\theta = 50°$

in the recirculation zones. A larger turbulent kinetic energy is seen on either side of the normally impinging jet and on the ground plane in Figure 8. Both sides of the jet flow were induced by the main jet flow. The induced fluid flow is dominated by viscous forces and the main jet flow is dominated by inertial forces; the larger turbulence fluctuation and kinetic energy for the two sides of the jet flow are produced by the interaction between these viscous and inertial forces. The larger turbulent kinetic energy zone appearing in the ground plane is due to flow deflection and acceleration. The turbulent energy dissipation rate contours are shown in Figure 9; the physical phenomena are the same as in Figure 8.

The streamlines of the obliquely impinging jet for $\theta = 80°$, 70° and 50° are shown in Figures 10–12 respectively. The sizes of the recirculation zones on the two sides of the jet change when the oblique impingement angle is decreased. The size of the left recirculation zone decreases and that of the right recirculation zone increases as θ is changed from 80° to 50°. Both recirculation zones

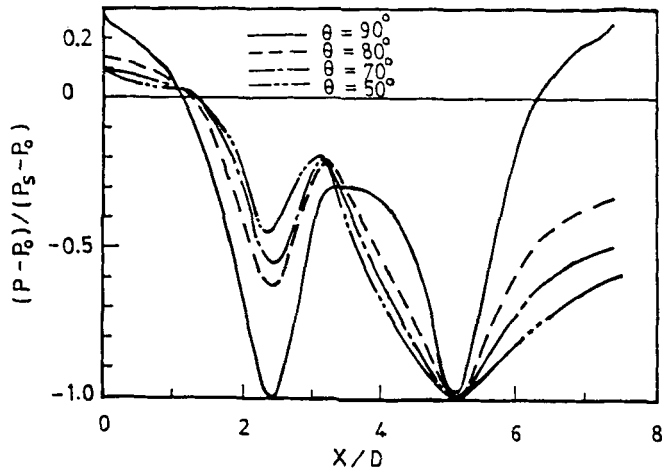

Figure 13. Upper plate surface pressure distributions for θ = 90°, 80°, 70°, 50°

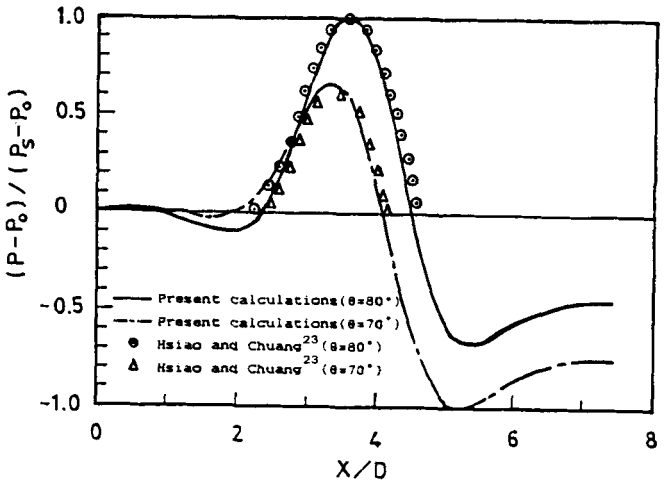

Figure 14. Ground plane pressure distributions for θ = 80°, 70°

at various oblique impingement angles satisfy energy conservation if we take the size of the recirculation zone as the value of the energy. The lift force of the upper plate increases with increasing oblique impingement angle as shown in Figure 13. The pressure distributions of the ground plane for $\theta = 80°$, 70° and 50° are shown in Figures 14 and 15. The calculated results of the ground plane pressure distributions for $\theta = 80°$ and 70° are compared with the experimental data of Hsiao and Chuang[23] in Figure 14 and found to be good in agreement. The maximum pressure location moves to the left and the value of the maximum pressure decreases as the oblique impingement angle is decreased. The pressure contours for $\theta = 80°$, 70° and 50° are shown in Figures 16–18 respectively. The maximum pressure zone moves to the left as θ changes from 80° to 50°. The pressure of the flow almost becomes negative when the oblique impingement angle is 50°. The turbulent kinetic energy of the impingement region gradually decreases as the oblique impingement angle is decreased owing to the smaller deflection for smaller oblique impingement angle, as shown in Figures 19–21. The size of the left recirculation zone gradually decreases due to compression by the obliquely impinging jet fluid flow and the turbulent kinetic

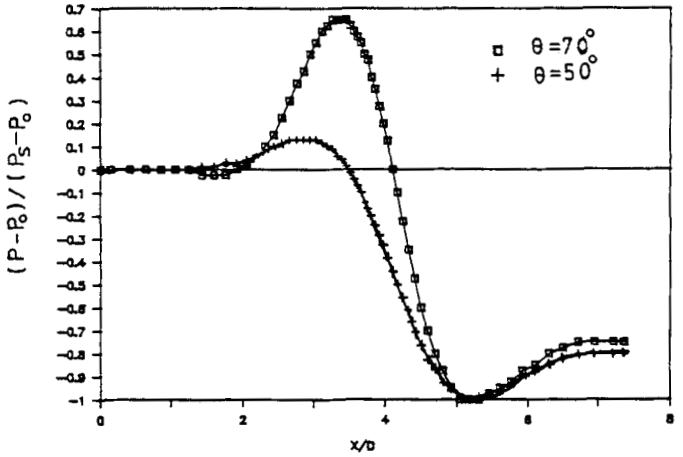

Figure 15. Ground plane pressure distributions for $\theta = 70°$, 50°

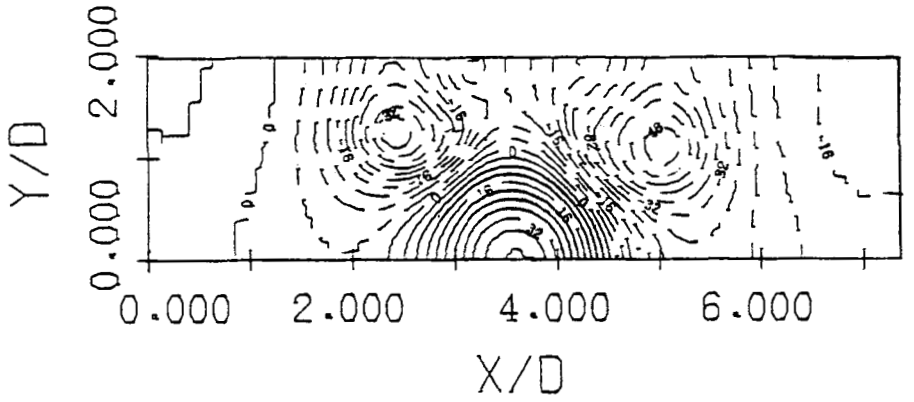

Figure 16. Pressure contours for $\theta = 80°$; broken lines indicate negative pressure

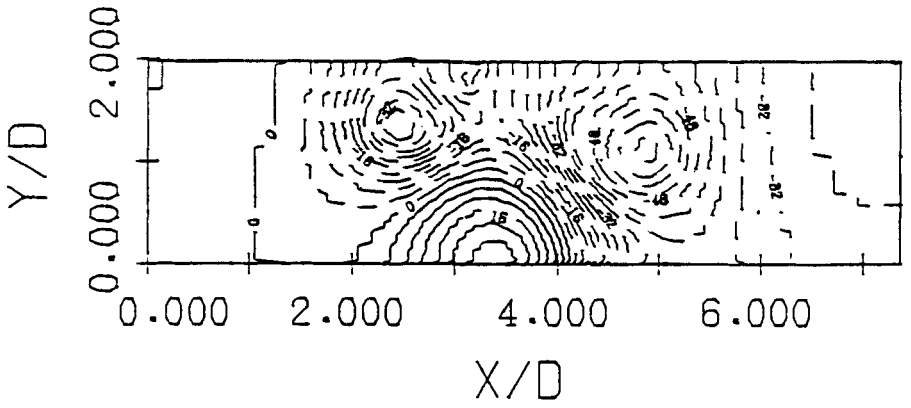

Figure 17. Pressure contours for $\theta = 70°$; broken lines indicate negative pressure

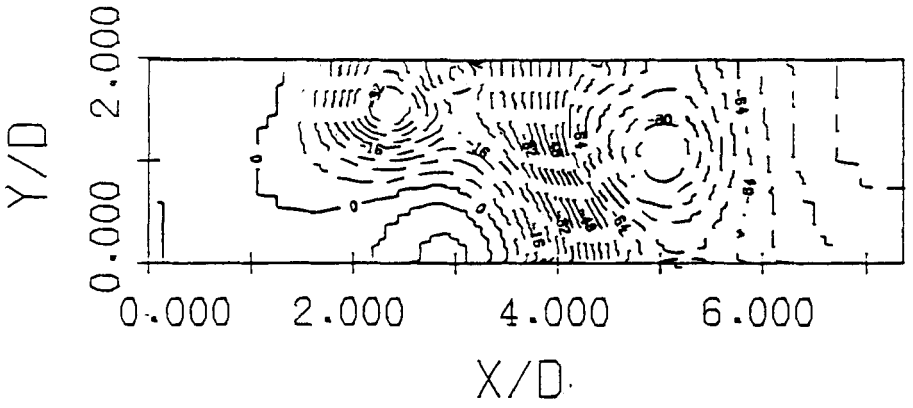

Figure 18. Pressure contours for $\theta = 50°$; broken lines indicate negative pressure

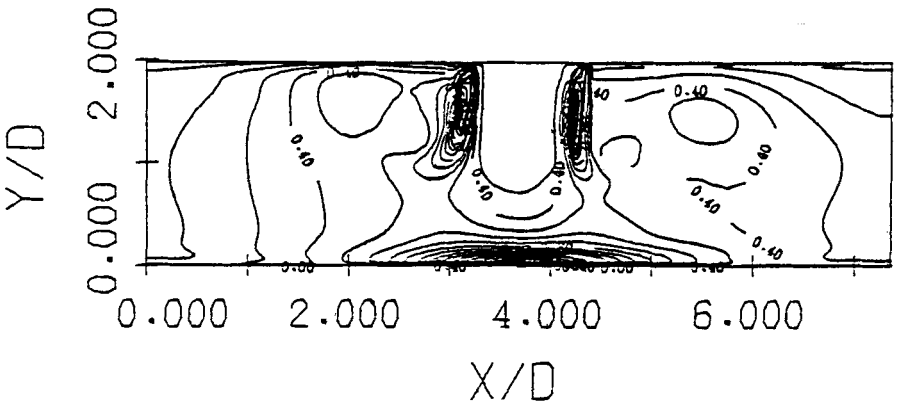

Figure 19. Turbulent kinetic energy contours for $\theta = 80°$

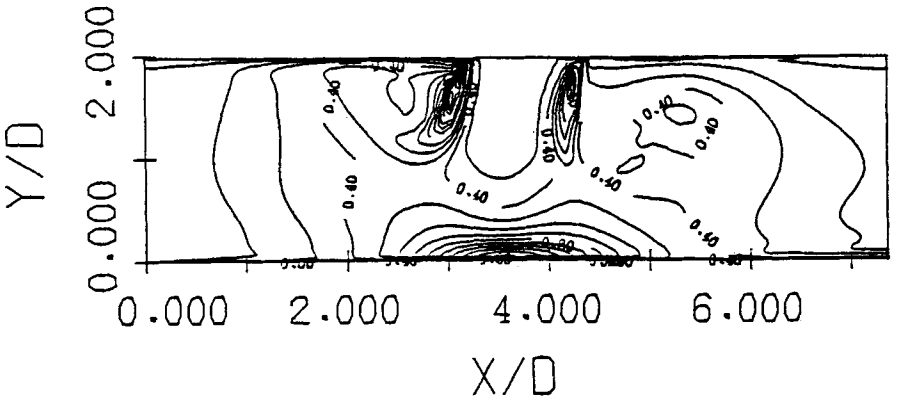

Figure 20. Turbulent kinetic energy contours for $\theta = 70°$

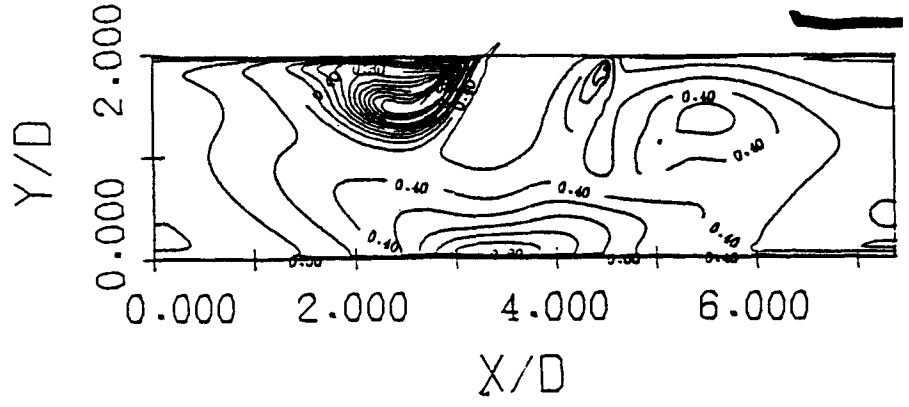

Figure 21. Turbulent kinetic energy contours for $\theta = 50°$

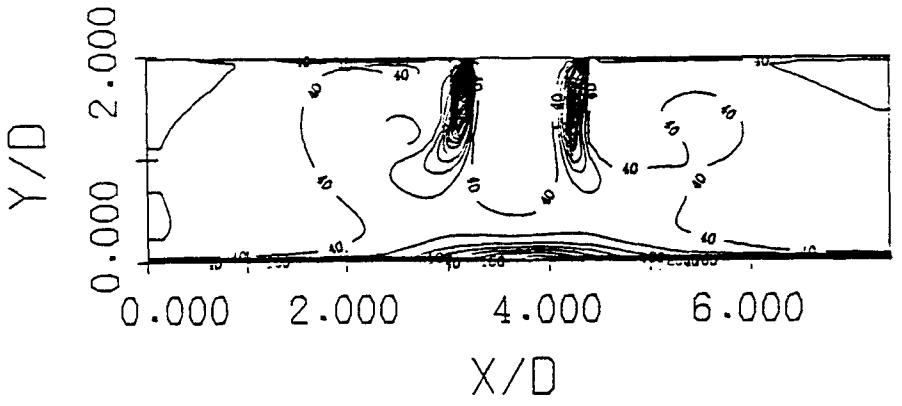

Figure 22. Turbulent energy dissipation rate contours for $\theta = 80°$

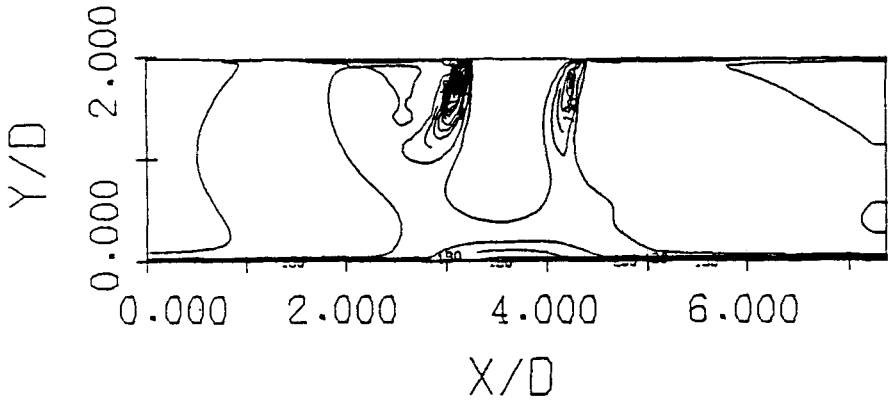

Figure 23. Turbulent energy dissipation rate contours for $\theta = 70°$

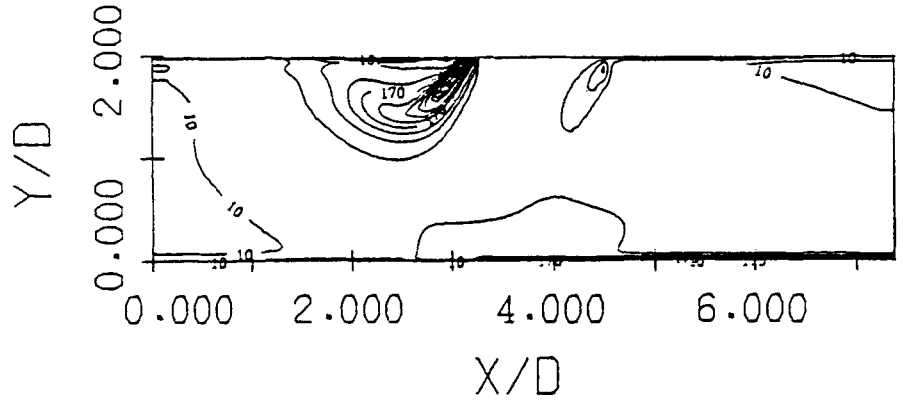

Figure 24. Turbulent energy dissipation rate contours for $\theta = 50°$

energy increases due to the interaction between inertial and viscous forces as the oblique impingement angle is decreased. In contrast, the size of the right recirculation zone increases and the turbulent kinetic energy decreases because the right recirculation zone is dominated by viscous forces. The turbulent energy dissipation rates for $\theta = 80°, 70°$ and $50°$ are shown in Figures 22–24 respectively. The physical phenomena of the turbulent energy dissipation rate for obliquely impinging jet flow are the same as those of the turbulent kinetic energy.

CONCLUDING REMARKS

1. The size of the left recirculation zone decreases and that of the right recirculation zone increases as the oblique impingement angle is decreased.
2. The maximum pressure zone moves to the left as the oblique impingement angle is decreased.
3. A larger loss of lift force is found for smaller oblique impingement angle.
4. For the turbulent kinetic energy, the left recirculation zone becomes larger and the right recirculation zone becomes smaller as the oblique impingement angle is decreased.

5. The turbulent energy dissipation rate shows the same physical trends as the turbulent kinetic energy when the oblique impingement angle is changed.
6. The SIMPLE-C algorithm has some important advantages; namely, no Jacobians of co-ordinate transformation and dissipation terms are necessary.

APPENDIX: NOMENCLATURE

A	surface area of control volume
a_i	joint coefficient
b	assumed mass source in pressure correction equation
C_1, C_2, C_μ	constants
D	diameter of nozzle
H	y/D
k	turbulent kinetic energy
Re	Reynolds number
S	source term of variable
S_p, S_c	coefficients of linearized source term
V_{in}	exit velocity of nozzle
u, v	velocity in the x- and y-direction respectively
W	x/D
Γ	transfer coefficient
ε	turbulent energy dissipation rate
μ_e	effective viscosity
μ_l	molecular viscosity
μ_t	eddy viscosity
ρ	density
ϕ	transport variable
θ	oblique impingement angle

REFERENCES

1. S. H. Chuang, 'Numerical simulation of an impinging jet on a flat plate', *Int. j. numer. methods fluids*, **9**, 1413–1426 (1989).
2. M. Wolfshtein, 'Some solutions of the plane turbulent impinging jet', *J. Basic Eng., Trans. ASME*, **92D**, 915–922 (1970).
3. D. D. Coleman, 'A study of free jet impinging, Part I, Mean properties of free and impinging jets', *J. Fluid Mech.*, **45**, 281–319 (1971).
4. V. Parameswaran and S. A. Alpay, 'Normal impingement of jets', *J. Aircraft*, **11**, 189–191 (1974).
5. M. J. Siclari, D. Migdal and J. L. Palcza, 'The development of theoretical models for jet-induced effects on V/STOL aircraft', *J. Aircraft*, **13**, 938–944 (1976).
6. M. J. Siclari, W. G. Hill Jr. and R. C. Jenkins, 'Investigation of stagnation line and upwash formation', *AIAA Paper 77-615*, Palo Alto, CA, 1977.
7. W. W. Bower and D. R. Kotansky, 'A Navier–Stokes analysis of the two-dimensional ground effects problem', *AIAA Paper 76-621*, 1976.
8. W. W. Bower, D. R. Kotansky and G. H. Hoffman, 'Computations and measurements of two-dimensional turbulent jet impingement flowfields', *Symp. Turbulent Shear Flows, Vol. 1*, University Park, Pa, 1977.
9. D. R. Kotansky and W. W. Bower, 'A basic study of the VTOL ground effect problem for planar flow', *J. Aircraft*, **15**, 214–221 (1978).
10. W. W. Bower, R. K. Agarwal and G. R. Peters, 'A theoretical study of two and three dimensional impinging jets', *MDRL 79-22*, 1979.
11. A. Rubel, 'Computations of jet impingement on a flat surface', *AIAA J.*, **18**, 168–175 (1980).
12. R. K. Agarwal and W. W. Bower, 'Navier–Stokes computations of turbulent compressible two-dimensional impinging jet flowfields', *AIAA J.*, **20**, 577–584 (1982).

13. M. K. Looney and J. J. Walsh, 'Mean-flow and turbulent characteristics of free and impinging jet flows', *J. Fluid Mech.*, **147**, 397–429 (1984).
14. R. W. MacCormack, 'The effect of viscosity in hypervelocity impact cratering', *AIAA Paper 69-354*, 1969.
15. R. W. MacCormack, 'Computational efficiency achieved by time splitting of finite difference operators', *AIAA Paper 72-154*, 1972.
16. R. M. Beam and R. F. Warming, 'An implicit factored scheme for the compressible Navier–Stokes equations', *AIAA J.*, **16**, 393–402 (1978).
17. T. H. Pulliam and J. L. Steger, 'On implicit finite difference simulations of three dimensional flows' *AIAA Paper 78-10*, 1978.
18. C. J. Hwang and J. L. Liu, 'Numerical study of two-dimensional impinging jet flowfields', *Proc. 4th Natl Conf. on Mechanical Engineering*, Chinese Society of Mechanical Engineering, Hsinchu, Taiwan, R.O.C., 1987, pp. 41–49.
19. R. W. MacCormack, 'A numerical method for solving the equations of compressible viscous flow', *AIAA Paper 81-0110*, 1981.
20. E. von Lavante and W. T. Thompkins Jr., 'An implicit bidiagonal numerical method for solving the Navier–Stokes equations', *AIAA J.*, **21**, 828–833 (1983).
21. J. P. van Doormaal and G. D. Raithby, 'Enhancements of the SIMPLE method for predicting incompressible fluid flows', *Numer. Heat Transfer*, **7**, 147–163 (1984).
22. R. Gardon and J. C. Akfirat, 'The role of turbulence in determining the heat-transfer characteristics of impinging jets', *Int. J. Heat Mass Transfer*, **8**, 1261–1272 (1965).
23. F. B. Hsiao and S. H. Chuang, 'A study of the reversed flow separation of the jet impingement on a varying angle plate', *NSC (R.O.C.) Report, Contract No. CS76-0210-D006-05*, 1988.
24. D. G. Lilley, 'Primitive pressure–velocity code for the computation of strongly swirling flow', *AIAA J.*, **14**, 749–756 (1976).
25. B. E. Launder and D. B. Spalding, *Lectures in Mathematical Models of Turbulence*, Academic Press, London, 1972.
26. S. V. Patankar, *Numerical Heat Transfer and Fluid Flow*, Hemisphere, New York, 1980.
27. B. R. Latimer and A. Pollard, 'Comparison of pressure–velocity coupling solution algorithms', *Numer. Heat Transfer*, **8**, 635–652 (1985).
28. S. H. Chuang and S. W. Lii, 'Combustion flowfield analysis of an afterburner with V-gutter flameholders', *Trans. The Aeronautical and Astronautical Society of the Republic of China* **21**, 39–54 (1988).
29. B. E. Launder and D. B. Spalding, 'The numerical computation of turbulent flows', *Comput. Methods Appl. Mech. Eng.*, **3**, 301–314 (1970).
30. W. P. Jones and B. E. Launder, 'The prediction of laminarization with a two-equation model of turbulence', *Int. J. Heat Mass Transfer*, **15**, 301–314 (1972).
31. H. S. Law and J. H. Masliyah, 'Numerical prediction of the flow field due to a continued laminar two-dimensional submerged jet', *Comput. Fluids*, **12**, 199–215 (1984).
32. A. R. P. van Heiningen, A. S. Mujumdar and W. J. M. Douglas, 'Numerical prediction of the flow field and impingement heat transfer due to a laminar slot jet', *Trans. ASME, J. Heat Transfer*, **98**, 654–658 (1976).